Research Square

Preprints are preliminary reports that have not undergone peer review.
They should not be considered conclusive, used to inform clinical practice,
or referenced by the media as validated information.

Risk-aware and trackability-constrained trajectory planning for autonomous vehicles in unstructured road environments

Xuan Yang
Shenyang Ligong University
Enjun Bai
ej_bai@yeah.net
Shenyang Ligong University
Jingsong Liu
Shenyang Ligong University
Maochen Ge
Shenyang Ligong University
Yongwang Chai
Shenyang Ligong University
Shuang Chen
Shenyang Ligong University
Wenyu Ma
Shenyang Ligong University

Article

Keywords: autonomous driving, unstructured roads, trajectory planning, risk-aware planning, dynamic obstacle avoidance, vehicle trackability

Posted Date: October 7th, 2026

DOI: https://doi.org/10.21203/rs.3.rs-11079930/v1

License: This work is licensed under a Creative Commons Attribution 4.0 International License.
Read Full License

Additional Declarations: No competing interests reported.

Risk-aware and trackability-constrained trajectory planning for autonomous vehicles in unstructured road environments

Xuan Yang[1], Enjun Bai[1,*], Jingsong Liu[1], Maochen Ge[1], Yongwang Chai[1], Shuang Chen[1], Wenyu Ma[1]
[1]Shenyang Ligong University, Shenyang, Liaoning, China
*Corresponding author: Enjun Bai; email: ej_bai@yeah.net

Abstract

Trajectory planning on unstructured roads must account for irregular boundaries, static and dynamic obstacles, and vehicle steering constraints. We present a risk-aware and trackability-constrained trajectory planning framework that integrates risk-sensitive path search, local replanning, curvature-constrained path optimization, spatio-temporal speed planning, and Hybrid A* replanning. Across four start-goal configurations on the same unstructured-road map, the proposed risk-aware search increased the mean obstacle-centre distance by 18.2% and reduced the risk integral and mean risk by 19.4% and 20.7%, respectively, compared with standard A*, while increasing the average path length by 1.5%. Subsequent B-spline optimization reduced the maximum path curvature from 0.2796 to 0.2074 m^{-1} and increased the minimum obstacle-centre distance from 1.1533 to 1.2927 m. Dynamic-obstacle simulations showed that transient conflicts could be resolved through speed adjustment, whereas persistent blockage was handled through local spatial replanning. Closed-loop CarSim/Simulink simulations further demonstrated accurate trajectory tracking without steering saturation. The framework reduced risk exposure while satisfying the tested geometric and vehicle-tracking constraints.

Keywords: autonomous driving; unstructured roads; trajectory planning; risk-aware planning; dynamic obstacle avoidance; vehicle trackability

Introduction

Autonomous driving technologies have achieved substantial progress in structured road environments, where lane markings, predefined road geometry and traffic regulations provide strong constraints for vehicle motion. In contrast, trajectory planning in unstructured road environments remains more challenging because explicit lane guidance is often unavailable and the drivable space may contain irregular boundaries, narrow passages and complex obstacle distributions. In such environments, an autonomous vehicle must find a collision-free route with sufficient safety margin and generate a trajectory that satisfies its motion constraints. Recent studies have identified terrain traversability assessment, cost estimation and terrain- and vehicle-dependent constraints as key issues in path planning for unstructured environments [1]. Trajectory-planning studies have further addressed collision-free and vehicle-feasible motion generation in complex unstructured free space [2].

Graph search and other established planning methods are widely used in autonomous driving to represent environmental and motion constraints explicitly [3]. The classical A* algorithm combines accumulated travel cost with a heuristic estimate to efficiently search for a minimum-cost path [4]. For car-like vehicles, Hybrid A* extends graph search into a continuous kinematic state space and can generate paths that satisfy nonholonomic vehicle constraints [5]. Improved A*-based methods have also been developed for different road types and vehicle-motion constraints [6]. However, when geometric distance is the dominant optimization objective, a path can be collision-free while still travelling close to obstacles or road boundaries. Such paths may satisfy a binary occupancy constraint but provide a limited safety margin against localization errors, modelling uncertainty or unexpected obstacle motion.

Risk-aware planning addresses this limitation by assigning continuous costs to environmental hazards rather than relying on binary collision checks alone. Risk-field approaches assign different costs to regions surrounding obstacles, road boundaries or other hazardous areas, allowing the planner to distinguish between routes with different levels of potential risk. Xia et al. introduced a geometric driver risk field for risk-oriented graph-search and optimization-based trajectory planning, enabling continuous evaluation of environmental risk during trajectory generation [7]. Tian et al. subsequently incorporated obstacle and road-boundary risk into autonomous-vehicle path and speed planning [8]. Recent studies have also investigated dynamically adjusted safety constraints based on online risk assessment [9], driving-safety-field methods that account for vehicle motion and kinematic characteristics [10], and hybrid trajectory planners that incorporate risk fields for static and moving obstacles in dynamic driving scenarios [11]. On unstructured road maps, a graph-based planner must balance cumulative risk and path length without losing connectivity through the available free space.

A collision-free path is not necessarily trackable by the vehicle. A grid-based planner may generate a geometrically valid path containing excessive curvature or rapid curvature variations that require steering inputs beyond the practical capability of the vehicle. Path smoothing is therefore commonly applied after graph search. B-spline curves are particularly suitable because of their geometric continuity and flexible control-point representation. Maekawa et al. demonstrated curvature-continuous path generation with explicit upper curvature bounds using B-spline curves [12], while more recent work has incorporated minimum-turning-radius constraints into B-spline smoothing for Ackermann-steered vehicles [13]. Nevertheless, curvature reduction cannot be considered independently of obstacle clearance. Moving a path during smoothing may reduce the distance to surrounding obstacles even when curvature is improved. Integrated planning-and-control studies have also combined trajectory generation with downstream tracking and vehicle-dynamics constraints to improve vehicle-level feasibility [14]. Curvature optimization within an explicitly defined safe corridor can address vehicle trackability and obstacle clearance together.

Dynamic obstacles introduce an additional challenge because a spatially feasible path may become unsafe as obstacle states evolve over time. Spatio-temporal (S-T) planning addresses this problem by coupling the longitudinal progress of the ego vehicle with time, enabling acceleration, deceleration or waiting to avoid predicted conflicts. Xin et al. showed that graph search and optimization can be combined in a spatio-temporal framework to generate smooth and dynamically feasible trajectories in constrained dynamic environments [15]. Related studies have addressed intention-aware planning around dynamic obstacles and fixed-path speed optimization through space-time conflict analysis [16,17]. Such temporal adjustment is effective when an obstacle occupies the planned path only temporarily. However, speed modification alone cannot solve every conflict. If an obstacle stops and persistently blocks the spatial corridor, delaying the ego vehicle does not restore geometric feasibility; a new path around the blockage must instead be generated. Hybrid A*, which explicitly considers vehicle kinematics during spatial search, provides an appropriate mechanism for this type of local replanning [5]. The choice between temporal adjustment and spatial replanning therefore depends on whether the predicted conflict is transient or persistent.

Risk-aware planning, path smoothing and dynamic trajectory planning are often investigated separately. For autonomous driving in unstructured road environments, a unified framework must address three related requirements: geometric search should consider cumulative environmental risk rather than collision avoidance alone; the resulting path should explicitly satisfy vehicle curvature and obstacle-clearance constraints; and dynamic conflicts should be handled differently depending on whether they represent transient temporal interactions or persistent spatial blockage. These requirements connect route selection to the vehicle's ability to follow the planned trajectory.

We propose a risk-aware and trackability-constrained trajectory planning framework for autonomous vehicles in unstructured road environments. An enhanced A* search includes environmental risk in the path cost while retaining a hard obstacle-clearance constraint. Safety-corridor-constrained B-spline optimization then reduces excessive curvature while preserving obstacle clearance. A hierarchical S-T/Hybrid A* strategy uses speed adjustment for transient conflicts and local spatial replanning for persistent blockage.

The framework was evaluated through comparative and ablation experiments and closed-loop CarSim/Simulink simulations. Figure 1 shows the occupancy-grid environment and the corresponding risk field used by the planner.

Results

Experimental setup

Experiments used a single unstructured occupancy map with a resolution of 0.5 m/cell. Four start-goal configurations were used to compare the search methods across different routes. For each scenario, three methods were compared:

Standard A* used a conventional eight-connected geometric cost and a Euclidean heuristic without the risk term, turning penalty or adaptive heuristic. Enhanced A* without risk used the proposed search framework but set $K_r = 0$. The proposed risk-aware A* retained the complete formulation with $K_r = 2.8$.

All methods used the same map, start and goal locations, obstacle representation and evaluation procedure.

Table 1 lists the main vehicle and planning parameters, and Table 2 summarizes performance across the four tasks. Figure 1 shows the common occupancy map and risk field. Figure 2 compares the paths for S1-S4, while Fig. 3 reports path length, mean obstacle-centre distance, risk integral and median search time for each task. Supplementary Table S4 lists the start-goal configurations.

Across S1-S4, the proposed method increased mean obstacle-centre distance in every task by 16.0-20.5% and reduced the risk integral by 16.8-22.6% relative to standard A* (Fig. 3b,c). Averaged across the four tasks, mean path length increased from 101.75 to 103.29 m (1.51%), whereas mean obstacle-centre distance increased from 1.9944 to 2.3572 m (18.2%), risk integral decreased from 29.462 to 23.754 (19.4%), and mean risk decreased from 0.29288 to 0.23227 (20.7%) (Table 2). The reduction in risk exposure was accompanied by a modest increase in mean path length.

The hard minimum-distance constraint was satisfied by all reported paths, but the proposed method did not maximize the minimum obstacle-centre distance in every scenario. In S2, its minimum distance was 1.1552 m compared with 1.1664 m for standard A*, while both remained above the 1.15 m hard threshold. The hard constraint limits the closest approach, whereas the risk term penalizes cumulative exposure along the route.

Risk-term ablation

To isolate the effect of environmental risk, the enhanced A* method with $K_r = 0$ and the proposed method with $K_r = 2.8$ were evaluated under identical search and post-processing conditions. The only difference between the two cases was the risk coefficient.

In the reference scenario, adding the risk term reduced the risk integral from 42.309 to 36.460 (13.8%) and the mean risk from 0.26581 to 0.23040 (13.3%). Mean obstacle-centre distance increased from 2.2020 to 2.4217 m (10.0%), while path length decreased slightly from 159.17 to 158.25 m (0.58%).

Because the turning penalty, adaptive heuristic and post-processing procedure were unchanged, the ablation isolates the contribution of the environmental-risk term. Supplementary Fig. S2 shows that the risk term changes the route during the raw search and that the difference persists after post-processing. Supplementary Fig. S1 shows the pathwise risk and obstacle-centre-distance profiles for the representative task.

Trackability optimization

The post-processed grid path was collision-free but exceeded the curvature limit for vehicle tracking. Prior to B-spline optimization, the maximum curvature was $0.279587\ m^{-1}$, which exceeded the 0.24 m^{-1} final tracking limit and was slightly above the measured vehicle curvature capability.

After safety-corridor-constrained B-spline optimization, the maximum curvature decreased to $0.207353\ m^{-1}$. The minimum obstacle-centre distance increased from 1.153256 to 1.292732 m. Path length increased from 158.556 to 161.040 m.

Maximum curvature decreased by approximately 25.8%, minimum obstacle-centre distance increased by 12.1%, and path length increased by 1.57%.

The path and curvature comparisons are shown in Fig. 4; the numerical before-and-after results are provided in Supplementary Table S1.

Dynamic-obstacle planning

Three dynamic obstacles were used to represent different types of dynamic conflict.

The conflict with O1 was resolved by decreasing vehicle speed so that the obstacle cleared the conflict region before the ego vehicle arrived. O2 represented a case where earlier passage was preferable, and the S-T planner increased vehicle speed while satisfying the imposed speed and dynamic limits. In contrast, O3 remained in the road after stopping. Since waiting could not restore spatial feasibility, the planner generated a new local geometric route using Hybrid A*, followed by a new S-T speed profile.

Dense evaluation of the final trajectory gave a minimum dynamic body-boundary distance of approximately 0.668 m, exceeding the prescribed 0.40 m requirement. In the sampled safety profiles shown in Supplementary Fig. S3, the minimum body-boundary distances for O1, O2 and O3 were 1.373, 0.670 and 1.589 m, respectively; all sampled values therefore remained above the same margin. Supplementary Fig. S3 visualizes the sampled separation distances; trajectory acceptance was determined by the planner's dense collision checks.

The final geometric path had a maximum curvature of approximately $0.231923\ m^{-1}$, below the strict 0.24 m^{-1} export limit. The maximum reference speed was approximately 2.60 m/s, and the complete manoeuvre lasted approximately 156.23 s. The maximum lateral acceleration was approximately 0.439 $m\ s^{-2}$, remaining within the conservative validation bound.

The spatial response and S-T planning results are shown in Fig. 5, and the final reference speed, longitudinal acceleration and jerk histories are shown in Fig. 6. The obstacle behaviours, selected strategies and outcomes are summarized in Supplementary Table S2. Supplementary Figs. S3 and S4 provide the sampled dynamic-separation check and the control-reference lateral-acceleration profile, respectively.

Closed-loop CarSim/Simulink validation

The final reference trajectory was tracked using a Simulink controller coupled with the CarSim vehicle model.

During the main tracking interval, from 0 to approximately 125 s, the maximum lateral tracking error was approximately $|e_y|_{\max} = 0.016$ m, and the maximum heading error was $|e_\psi|_{\max} = 1.29°$.

Over the complete trajectory, including the low-speed terminal phase, the maximum lateral error was 0.0678 m and the maximum heading error was $2.470°$. The final geometric position error relative to the reference goal was approximately 0.1117 m.

The maximum commanded equivalent front-wheel angle was approximately $26.08°$, below the available steering capability, and no steering saturation occurred. The curvature constraints imposed during planning were therefore compatible with the simulated vehicle's steering capability.

Supplementary Table S3 summarizes the closed-loop tracking errors.

Discussion

The experiments assess risk-aware route selection, curvature-constrained path optimization, dynamic-obstacle handling and closed-loop trajectory tracking.

The comparison across the four tasks shows that the risk term primarily changes how the route is distributed through feasible free space rather than simply maximizing the minimum obstacle-centre distance. Figure 3 shows a consistent increase in mean obstacle-centre distance and reduction in accumulated risk across all four tasks, while the minimum-distance metric changes only modestly and is slightly lower in S2. The 1.15 m threshold limits the closest approach, while the continuous risk field penalizes sustained exposure to higher-risk regions. The representative profiles in Supplementary Fig. S1 illustrate the same distinction along the path.

Reducing risk exposure increased the computational cost of the search. Relative to standard A*, the proposed method increased the mean expanded-node count from 2557.8 to 3561.5 (approximately 39%) and increased the mean of the scenario-wise median search times from 0.626 to 1.555 s, about 2.5 times the baseline value (Table 2). The scenario-level timing pattern is shown in Fig. 3d. The improvement concerns risk exposure rather than search speed.

The B-spline experiment shows why collision-free geometry alone is insufficient for vehicle tracking. The pre-optimization path had a maximum curvature of 0.2796 m^{-1}, whereas safety-corridor-constrained B-spline optimization reduced this value to 0.2074 m^{-1} (25.8%). At the same time, the minimum obstacle-centre distance increased from 1.1533 to 1.2927 m (12.1%), with a 1.57% increase in path length. The optimized path remained within the evaluated free-space corridor, so curvature reduction did not come at the expense of obstacle clearance in this case (Fig. 4).

Temporal and spatial replanning address different types of conflict. When the geometric corridor remains available and the conflict is temporary, S-T speed planning can resolve the interaction without changing the spatial route; when a stopped obstacle persistently blocks the spatial route, local Hybrid A* replanning is required (Fig. 5). The resulting reference trajectory also satisfies the imposed speed, longitudinal-acceleration and jerk bounds (Fig. 6), while Supplementary Fig. S4 shows that the control-reference lateral acceleration remains within the nominal ±0.50 m/s² limits. Supplementary Fig. S3 provides a sampled visualization of body-boundary separation and should not be interpreted as a continuous-time collision certificate; dense trajectory-level collision checking remains the acceptance criterion.

The CarSim/Simulink simulations test closed-loop tracking, rather than only the reference-trajectory limits shown in Fig. 6 and Supplementary Fig. S4. The small lateral and heading tracking errors and the absence of steering saturation indicate that the curvature limits imposed during planning are consistent with the simulated vehicle steering capability. These results support vehicle tracking in simulation, but do not establish performance on a physical vehicle.

The principal limitation is computational performance. The current MATLAB prototype requires tens of minutes of computation for the complete multi-stage planning and validation workflow, and the core planning computation in the reference experiment was approximately 30.5 min. The current implementation demonstrates planning feasibility and closed-loop tracking, not real-time operation. Evaluation was also limited to one unstructured occupancy map with four start-goal configurations. Performance on substantially different terrain and obstacle layouts remains to be tested.

Future work should focus on incremental risk-field updates, more efficient open-set data structures, accelerated collision checking, warm-started optimization and parallelization, together with evaluation on additional map topologies. Hardware-in-the-loop and physical-vehicle tests will be required to assess robustness to perception uncertainty, obstacle-prediction errors, road-surface effects and actuator delays. The current deterministic obstacle predictions could also be extended with probabilistic motion models to represent uncertainty in surrounding-object behaviour explicitly.

The tested framework links risk-aware route selection, curvature-constrained path optimization and conflict-dependent replanning. Across the four planning tasks, the proposed search increased mean obstacle-centre distance by 18.2% and reduced the risk integral by 19.4% with a 1.5% increase in mean path length; the subsequent B-spline stage reduced maximum curvature by 25.8% while increasing minimum obstacle-centre distance by 12.1%. Closed-loop simulation then showed that the resulting reference could be tracked without steering saturation. Within the tested simulations, the planning constraints were compatible with closed-loop vehicle tracking.

Methods

Problem formulation and environment representation

Autonomous trajectory planning in an unstructured road environment is formulated as finding a collision-free, trackable trajectory between initial and target configurations in a bounded two-dimensional workspace. No predefined lane centreline is assumed, and the vehicle therefore determines its route directly from the available free space.

The environment is represented using a binary occupancy grid. The original map contains 60×100 cells with a nominal resolution of 1.0 m/cell. To improve spatial resolution for collision checking and trajectory optimization, the map is refined to 120×200 cells using nearest-neighbour refinement, with $\Delta = 0.5$ m/cell.

Each original cell is expanded into a 2×2 block, thereby preserving the obstacle topology of the original map.

Grid coordinates are represented as $\mathbf{q} = [r, c]^{\mathrm{T}}$, where r and c correspond to the physical y- and x-directions, respectively. Physical coordinates are converted according to equation (1).

$$r = \mathrm{round}\left(\frac{y}{\Delta}\right), \qquad c = \mathrm{round}\left(\frac{x}{\Delta}\right). \tag{1}$$

The reference scenario uses $(x_s, y_s) = (8,12)$ m and $(x_g, y_g) = (2,41)$ m, corresponding to grid coordinates $[24,16]$ and $[82,4]$.

Let $\mathcal{G} = \mathcal{G}_{\mathrm{free}} \cup \mathcal{G}_{\mathrm{obs}}$ denote the complete workspace. The path and its feasibility conditions are expressed as

$$\begin{gathered} \mathcal{P} = \{\mathbf{q}_0, \mathbf{q}_1, \dots, \mathbf{q}_N\}, \\ \mathbf{q}_i \in \mathcal{G}_{\mathrm{free}}, \qquad d(\mathbf{q}_i, \mathcal{G}_{\mathrm{obs}}) \geq d_{\mathrm{safe}}. \end{gathered} \tag{2}$$

A temporary static obstacle is represented as a rectangular occupied region. In the reference scenario, it has a size of 2.0×1.0 m and is centred at $[y, x] = [13,26]$ m. It is excluded from the initial global search and introduced subsequently to evaluate local replanning.

Environmental risk is represented using a quadratic distance-decay function

$$C(d; d_{\mathrm{th}}) = \left[\max\left(0, 1 - \frac{d}{d_{\mathrm{th}}}\right)\right]^2. \tag{3}$$

The distance field is calculated from the nearest obstacle, the workspace boundary and the available local clearance.

Vehicle and safety constraints

The planning constraints are derived from the same vehicle model used in the subsequent CarSim validation. The vehicle length, width and wheelbase are 3.8, 1.6 and 2.0 m, respectively, and the front track width is 1.38 m.

Steady-state steering-rack tests in CarSim gave measured maximum path curvatures of $+0.278852$ and -0.278852 m^{-1}. The physical curvature capability is therefore $\kappa_{\text{phy}} = 0.278852$ m^{-1}.

For an equivalent bicycle model, curvature is related to the equivalent front-wheel angle as follows. A safety coefficient of 0.95 is applied to the measured physical curvature:

$$\kappa = \frac{\tan\delta}{L}, \qquad \kappa_{\text{plan}} = 0.95\kappa_{\text{phy}} = 0.264909 \text{ m}^{-1}. \tag{4}$$

where L is the wheelbase and δ is the equivalent front-wheel angle.

The final trajectory optimization target is $\kappa_{\text{target}} = 0.23$ m^{-1}, and the strict export limit is $|\kappa(s)| \leq 0.24$ m^{-1}, while the Hybrid A* search uses 0.235 m^{-1}. These limits reserve steering capacity for closed-loop correction.

The required static obstacle-centre clearance is

$$d_{\text{static}} = \frac{W}{2} + \frac{\Delta}{2} + m_{\text{static}} = 1.15 \text{ m}. \tag{5}$$

where $W = 1.6$ m, $\Delta = 0.5$ m and $m_{\text{static}} = 0.10$ m.

The final continuous path is always checked against this full requirement, even if the discrete search temporarily uses a slightly relaxed inflation radius to preserve connectivity.

Dynamic-obstacle checking uses the complete vehicle envelope and an additional boundary margin $m_{\text{dyn}} = 0.40$ m. Hence,

$$d_{\text{body}}\left(\mathcal{B}_{\text{ego}}, \mathcal{B}_{\text{obs}}\right) \geq m_{\text{dyn}}. \tag{6}$$

The cruise and maximum speeds are 1.60 and 2.60 m/s, respectively. The longitudinal acceleration, deceleration, lateral acceleration and jerk limits are 1.20 m s^{-2}, 1.00 m s^{-2}, 0.50 m s^{-2} and 3.00 m s^{-3}.

A curvature-dependent speed limit is imposed according to

$$a_y = v^2|\kappa|, \qquad v_\kappa(s) \leq \sqrt{\frac{a_{y,\max}}{|\kappa(s)|}}. \tag{7}$$

Risk-aware A* path planning

The environmental risk associated with a free grid cell n is formed from obstacle, boundary and narrow-passage risk:

$$\begin{gathered}\tilde{R}(n) = w_{\text{obs}}C(d_{\text{obs}}) + w_{\text{bound}}C(d_{\text{bound}}) + w_{\text{narrow}}C(d_{\text{clear}}), \\ d_{\text{clear}} = \min(d_{\text{obs}}, d_{\text{bound}}).\end{gathered} \tag{8}$$

The influence ranges are 5.0 m for obstacle risk, 4.0 m for boundary risk and 3.5 m for narrow-passage risk. Their respective weights are 0.65, 0.30 and 0.35. The resulting risk field is normalized over traversable cells.

For a transition from n_i to n_j, the motion cost and the risk-augmented cumulative path cost are

$$\begin{aligned} J_{\text{move}} &= l_{ij}\left[1 + \lambda_{\text{turn}}\left(1 - \cos\theta_{ij}\right)\right], \\ g\left(n_j\right) &= g(n_i) + J_{\text{move}} + K_r R\left(n_j\right). \end{aligned} \tag{9}$$

where $l_{ij} = 1$ or $\sqrt{2}$ for axial and diagonal moves and $\lambda_{\text{turn}} = 0.1$, with $K_r = 2.8$. The search therefore penalizes cumulative exposure to risky regions rather than only checking binary collision feasibility.

An adaptive heuristic combines Euclidean distance, direction consistency and Manhattan distance:

$$\begin{gathered} h = \alpha H_{\text{dist}} + \beta H_{\text{dir}} + \gamma H_{\text{exp}}, \qquad f(n) = g(n) + h(n), \\ H_{\text{dist}} = \| n - n_g \|_2 , \qquad H_{\text{dir}} = 1 - \cos\phi, \\ H_{\text{exp}} = \left|r - r_g\right| + \left|c - c_g\right|. \end{gathered} \tag{10}$$

For normalized search progress $\xi = \min\left(N_{\text{exp}}/5000, 1\right)$, the adaptive weights are

$$\alpha = 0.1(1 - \xi), \qquad \beta = 0.05 + 0.1\xi, \qquad \gamma = 1.5(1 - \xi). \tag{11}$$

Candidate nodes are ranked by $f(n)$. The planner uses eight-connected expansion, and diagonal transitions that would cut through occupied corners are rejected.

The $K_r = 0$ ablation retains the same turning penalty and adaptive heuristic and is therefore denoted Enhanced A* without risk, rather than standard A*.

Local replanning for newly appearing static obstacles

The initial global route is generated without the temporary static obstacle. When the obstacle is introduced into the planning map, the reference path is first resampled at approximately 0.20 m intervals. The distance from each sampled path point to the temporary obstacle is then evaluated. A conflict region is declared when the centreline distance is less than the strict static-clearance requirement plus an additional 0.80 m influence range.

Instead of replanning the complete global route, points located before and after the affected segment are selected as local connection points. Progressively larger local windows are attempted if the first window does not contain a feasible detour. Cells outside the selected window are temporarily treated as occupied so that the search remains spatially local. The temporary obstacle, fixed obstacles and local-window boundaries are incorporated into the local map.

The same risk-aware A* formulation is then used between the local entry and exit points. The reconstructed path is simplified by removing nearly collinear nodes only when the replacement line segment remains safe. Collision-constrained discrete smoothing is then applied in the forward and backward directions. The replanned segment is finally joined with the unaffected prefix and suffix of the original path, and adjacent duplicate points are removed.

This local strategy avoids unnecessary modification of the complete global path when a newly detected static obstacle affects only a limited path section.

Trackability-constrained B-spline optimization

Although the risk-aware search provides a safe route, grid discretization and local replanning can generate curvature peaks that are unsuitable for direct vehicle tracking. Curvature-constrained B-spline optimization is therefore applied before dynamic-obstacle processing.

Rather than freely optimizing two-dimensional control points, the proposed method represents the optimized path as a lateral displacement from the risk-aware reference path:

$$\begin{aligned} \mathbf{p}(s) &= \mathbf{p}_{\text{ref}}(s) + \mathbf{n}(s)d(s), \\ d(s) &= \textstyle\sum_{j=1}^{N_c} B_j(s) z_j. \end{aligned} \tag{12}$$

Here, $\mathbf{n}(s)$ is the local path normal, and $d(s)$ is represented by a cubic B-spline. This formulation preserves the basic topology selected by the risk-aware A* planner while allowing the curve to move within the available free-space corridor.

The control-point spacing is approximately 2.75 m, with 12–64 control variables depending on path length. The first and last three controls are fixed at zero displacement to preserve the start and terminal geometry. The path and constraints are evaluated at 0.10 m intervals.

At each reference point, the permissible displacement is determined separately in the positive and negative normal directions. The search stops before either the strict obstacle-clearance constraint or the map boundary would be violated. This creates an asymmetric safety corridor

$$-d_i^- \le d(s_i) \le d_i^+. \tag{13}$$

The maximum lateral corridor search width is 4.5 m, with a 0.10 m search step and a 0.03 m reserve.

The optimization objective is

$$\begin{aligned} J = {} & w_r J_{\text{ref}} + w_2 J_2 + w_3 J_3 + w_e J_{\kappa,e} \\ & + w_\kappa J_\kappa + w_{\dot{\kappa}} J_{\dot{\kappa}} + w_l J_l + w_c J_c. \end{aligned} \tag{14}$$

where the individual terms penalize deviation from the reference path, second- and third-order offset variations, curvature exceeding the target, total curvature energy, curvature variation, path-length increase and reduced obstacle clearance.

The weights $(w_r, w_2, w_3, w_e, w_\kappa, w_{\dot{\kappa}}, w_l, w_c)$ are (0.8, 45, 14, 12,000, 12, 120, 3, 25), respectively.

The nonlinear curvature and clearance constraints are

$$|\kappa_i| \le \kappa_{\text{lim}}, \qquad d_{\text{obs},i} \ge d_{\text{static}}. \tag{15}$$

Map-boundary and maximum-length constraints are also imposed. A small numerical curvature margin of 0.001 m^{-1} is retained below the final hard limit.

The optimization is solved with sequential quadratic programming in fmincon. Multiple initial solutions are tested, including zero lateral displacement and smooth outward displacements of 0.65 and 1.20 m around the dominant curvature region.

A solution is accepted only if it remains within the map, satisfies the clearance and physical-curvature constraints, has a path length no greater than 1.12 times that of the original path, and either reaches the curvature target or produces a meaningful curvature improvement. If the B-spline stage cannot produce an acceptable path for tracking, local Hybrid A* replanning can be used around the curvature-critical region rather than replanning the whole route.

Hierarchical dynamic-obstacle planning

Dynamic obstacles are represented by their initial position, dimensions, velocity and active lifetime. Collision prediction is performed using the full vehicle envelope rather than a point representation. The planner repeatedly detects the earliest unresolved conflict, attempts temporal resolution using S-T planning, and activates Hybrid A* spatial replanning only when temporal adjustment is insufficient. The numerical obstacle configurations are provided in Supplementary Table S5.

S-T speed planning

The spatial path is parameterized by arc length s, giving an S-T state $\mathbf{z} = [s, t]^{\mathrm{T}}$. The discretization is $\Delta t = 0.5$ s and $\Delta s = 0.20$ m.

Local S-T optimization is normally performed over a spatial window extending 24 m before and 22 m after the predicted conflict.

Dynamic programming (DP) is first used to select a feasible progress sequence. The generic stage cost can be written as

$$J_{\mathrm{DP}} = w_r J_r + w_w J_w + w_v J_v + w_a J_a + w_t J_t + w_l J_{\mathrm{lag}} + w_s J_{\mathrm{stop}}. \tag{16}$$

where obstacle risk, warning-zone occupancy, deviation from reference velocity, acceleration, travel time, progress lag and premature stopping are penalized. The implemented weights are 18, 36, 0.80, 4.5, 0.085, 0.35 and 16, respectively. Forward progress is constrained to be non-negative, allowing explicit stationary waiting states, and acceleration/deceleration bounds are enforced.

The DP result is subsequently smoothed using quadratic programming (QP). For the progress vector $\mathbf{s}$,

$$\begin{aligned} J_{\mathrm{QP}} = w_{\mathrm{ref}} \parallel \mathbf{s} - \mathbf{s}_{\mathrm{DP}} \parallel^2 + w_v \parallel D_1 \mathbf{s} \parallel^2 \\ + w_a \parallel D_2 \mathbf{s} \parallel^2 + w_j \parallel D_3 \mathbf{s} \parallel^2. \end{aligned} \tag{17}$$

where D_1, D_2 and D_3 approximate velocity, acceleration and jerk. The corresponding weights are 1, 1, 120 and 350.

The QP is subject to monotonic progress, path-dependent velocity limits, longitudinal acceleration/deceleration limits and jerk constraints:

$$\begin{aligned} 0 \le \dot{s} \le v_{\mathrm{lim}}(s), \\ -d_{\max} \le \ddot{s} \le a_{\max}, \quad |\dddot{s}| \le j_{\max}. \end{aligned} \tag{18}$$

A collision-free S-T corridor provides lower and upper spatial bounds at each time step.

The allowable velocity is additionally reduced in curved sections. A conservative lateral-acceleration value $a_{y,\mathrm{safe}} = 0.88 \times 0.50 = 0.44$ m s^{-2} is used to construct the curvature-dependent speed envelope. Forward acceleration and backward braking envelopes are applied so that the vehicle begins to decelerate before entering a high-curvature region.

Hybrid A* spatial replanning

If the conflicting obstacle remains permanently after stopping, temporal waiting cannot recover spatial feasibility. Such conflicts are therefore sent directly to Hybrid A* replanning. Similarly, Hybrid A* is activated when an S-T solution remains infeasible or still causes a body-envelope conflict after validation.

Hybrid A* uses the full 3.8×1.6 m vehicle footprint and a search curvature limit of 0.235 m^{-1}. The motion-primitive step is 0.50 m, and curvature at the terminal and path-connection regions is checked at a finer 0.10 m spacing.

For a persistent obstacle, its final stopped position is converted into a static occupied region during local spatial replanning. Progressively larger local windows are tested to provide sufficient turning space without unnecessarily changing the entire route.

After successful Hybrid A* replanning, the connection regions are subjected to additional curvature smoothing. The spatial path is then returned to the S-T planner, where the speed profile is recomputed using the new geometry and curvature-dependent limits.

Rolling commitment of resolved conflicts

After a dynamic obstacle has been safely passed, the already executed or safety-critical S-T prefix is frozen. Later obstacle handling may modify only the remaining suffix. This prevents later replanning from reintroducing a conflict with an earlier obstacle.

The committed state stores the corresponding s, t and velocity histories, and later plans are checked to confirm that the frozen prefix remains unchanged.

Generation of the vehicle-level reference trajectory

After geometric and dynamic planning, the S-T trajectory undergoes a final strict processing stage. This stage preserves the planned acceleration, deceleration and waiting sequence, enforces Hybrid-segment speed limits, sets the initial and terminal reference velocities to zero, and rechecks dynamic-obstacle safety and vehicle dynamics.

The final reference is uniformly resampled at $T_s = 0.05$ s and exported as $\mathtt{refTraj} = [t, x, y, \psi, \kappa, v, a, s]$. The units are seconds for time, metres for the two position coordinates, radians for heading, m^{-1} for curvature, m/s for speed, m s^{-2} for acceleration and metres for path length.

The final trajectory is supplied to the Simulink tracking controller and the CarSim vehicle model to evaluate tracking with vehicle dynamics and steering actuation.

Closed-loop tracking controller

Closed-loop validation used a lateral model predictive controller (MPC) based on a linear bicycle prediction model together with a longitudinal station-speed cascade controller. The lateral MPC tracked the rear-axle reference and generated the equivalent front-wheel steering command, while an outer station-error loop adjusted the desired speed and an inner proportional-integral-derivative (PID) speed loop generated the longitudinal acceleration command. The steering and acceleration commands were subsequently mapped to the CarSim steering-wheel, throttle and brake inputs. The main vehicle-model and closed-loop controller parameters are listed in Supplementary Table S6. The controller was used to validate the planned trajectory and was not a methodological contribution of this study.

Simulation and computational setup

All trajectory-planning algorithms were implemented in MATLAB R2024a and executed on a computer running Windows 11 with an Intel Core i5-13400F processor and 32 GB of RAM. Vehicle-level closed-loop simulations were conducted using MATLAB/Simulink R2024a coupled with CarSim 2021.0. For each start-goal configuration, each search method was executed five times, and the median search time was reported to reduce the influence of run-to-run variation.

Use of generative AI tools

During manuscript preparation, the authors used ChatGPT (OpenAI) to assist with English-language editing and wording refinement. All scientific content, analyses, interpretations and the final text were reviewed and approved by the authors, who take full responsibility for the manuscript.

Code availability

The custom MATLAB code used to implement the proposed trajectory-planning framework and generate the results reported in this study is available from the corresponding author on reasonable request.

Data availability

The datasets generated and analysed during the current study are available from the corresponding author on reasonable request.

References

[1] Wang, N., Li, X., Zhang, K., Wang, J. & Xie, D. A survey on path planning for autonomous ground vehicles in unstructured environments. *Machines* **12**, 31 (2024). DOI: 10.3390/machines12010031.

[2] Essuman, J. B. & Meng, X. Optimal trajectory planning for autonomous vehicles in unstructured environments. IEEE Control Syst. Lett. 8, 2673–2678 (2024). DOI: 10.1109/LCSYS.2024.3510359.

[3] Reda, M., Onsy, A., Haikal, A. Y. & Ghanbari, A. Path planning algorithms in the autonomous driving system: A comprehensive review. *Robot. Auton. Syst.* **174**, 104630 (2024). DOI: 10.1016/j.robot.2024.104630.

[4] Hart, P. E., Nilsson, N. J. & Raphael, B. A formal basis for the heuristic determination of minimum cost paths. *IEEE Trans. Syst. Sci. Cybern.* **4**, 100–107 (1968).

[5] Dolgov, D., Thrun, S., Montemerlo, M. & Diebel, J. Path planning for autonomous vehicles in unknown semi-structured environments. *Int. J. Robot. Res.* **29**, 485–501 (2010). DOI: 10.1177/0278364909359210.

[6] Zhou, X., Pei, X. & Yang, B. Hierarchical hybrid trajectory planning for autonomous vehicle considering multiple road types. *Proc. Inst. Mech. Eng. D J. Automob. Eng.* **237**, 2217–2230 (2023). DOI: 10.1177/09544070221107224.

[7] Xia, T., Chen, H., Yang, J. & Guo, Z. Geometric field model of driver's perceived risk for safe and human-like trajectory planning. *Transp. Res. C Emerg. Technol.* **159**, 104470 (2024). DOI: 10.1016/j.trc.2023.104470.

[8] Tian, G., Chang, T. & Fan, Y. A risk field-based trajectory planning method for autonomous vehicles to enhance real-time performance, safety, and traffic efficiency. *Proc. Inst. Mech. Eng. D J. Automob. Eng.* **240**, 4400–4416 (2026). DOI: 10.1177/09544070251357149.

[9] Zhao, J., Yan, X., Zhou, Z. & Zhang, Z. Rule-adaptive lane-changing trajectory planning method for autonomous vehicles driven by dynamic risk information. *Sci. Rep.* **15**, 31514 (2025). DOI: 10.1038/s41598-025-15382-1.

[10] Liu, K., Wang, H., Fu, Y., Wen, G. & Wang, B. A dynamic path-planning method for obstacle avoidance based on the driving safety field. Sensors 23, 9180 (2023). DOI: 10.3390/s23229180.

[11] Wang, M., Zhang, L., Zhang, Z. & Wang, Z. A hybrid trajectory planning strategy for intelligent vehicles in on-road dynamic scenarios. IEEE Trans. Veh. Technol. 72, 2832–2847 (2023). DOI: 10.1109/TVT.2022.3215476.

[12] Maekawa, T., Noda, T., Tamura, S., Ozaki, T. & Machida, K. Curvature continuous path generation for autonomous vehicle using B-spline curves. *Comput. Aided Des.* **42**, 350–359 (2010). DOI: 10.1016/j.cad.2009.12.007.

[13] Huo, F., Zhu, S., Dong, H. & Ren, W. A new approach to smooth path planning of Ackerman mobile robot based on improved ACO algorithm and B-spline curve. *Robot. Auton. Syst.* **175**, 104655 (2024). DOI: 10.1016/j.robot.2024.104655.

[14] Gao, Y., Li, D., Sui, Z. & Tian, Y. Trajectory planning and tracking control of autonomous vehicles based on improved artificial potential field. IEEE Trans. Veh. Technol. 73, 12468–12483 (2024). DOI: 10.1109/TVT.2024.3389054.

[15] Xin, L. et al. Enable faster and smoother spatio-temporal trajectory planning for autonomous vehicles in constrained dynamic environment. *Proc. Inst. Mech. Eng. D J. Automob. Eng.* **235**, 1101–1112 (2021). DOI: 10.1177/0954407020906627.

[16] Benciolini, T., Wollherr, D. & Leibold, M. Non-conservative trajectory planning for automated vehicles by estimating intentions of dynamic obstacles. IEEE Trans. Intell. Veh. 8, 2463–2481 (2023). DOI: 10.1109/TIV.2023.3234163.

[17] Shi, X. & Li, X. Trajectory planning for an autonomous vehicle with conflicting moving objects along a fixed path – an exact solution method. Transp. Res. B Methodol. 173, 228–246 (2023). DOI: 10.1016/j.trb.2023.05.001.

Funding

This work was supported by the Basic Scientific Research Project of Liaoning Provincial Department of Education (No. LJ212410144017).

Author contributions

All authors contributed to the conception and development of the study, analysis and interpretation of the results, and preparation and revision of the manuscript. All authors reviewed and approved the final manuscript.

Additional information

Competing interests

The authors declare no competing interests.

Figure legends

Figure 1. Environment representation and environmental risk field. a, Refined binary occupancy map for the reference unstructured-road scenario, with start and goal positions. b, Normalized environmental risk field constructed from obstacle, boundary and narrow-passage terms. Axis coordinates are given in metres and the refined grid resolution is 0.5 m/cell.

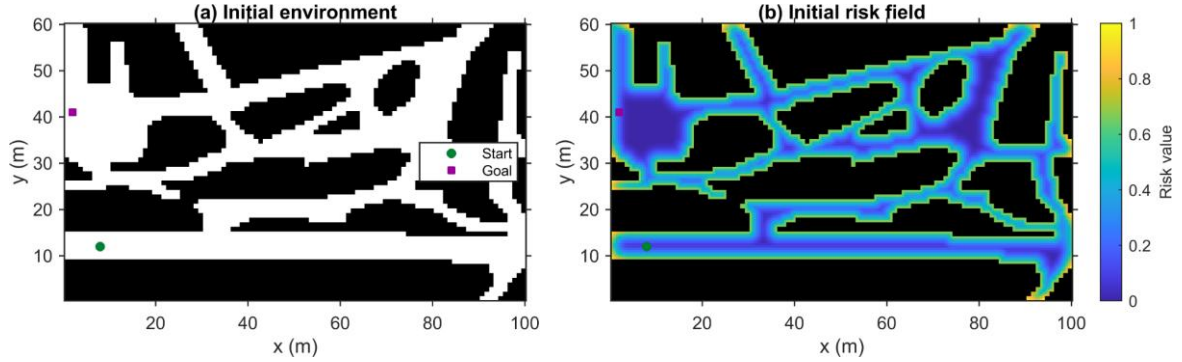


Figure 2. Path-planning comparisons for four start-goal configurations. a-d, Tasks S1-S4, respectively. Each panel compares the post-processed paths obtained with standard A*, enhanced A* without risk ($K_r = 0$), and the proposed risk-aware A* ($K_r = 2.8$) on the same occupancy map. Start and goal positions are identified in each panel, and both axes use metres.

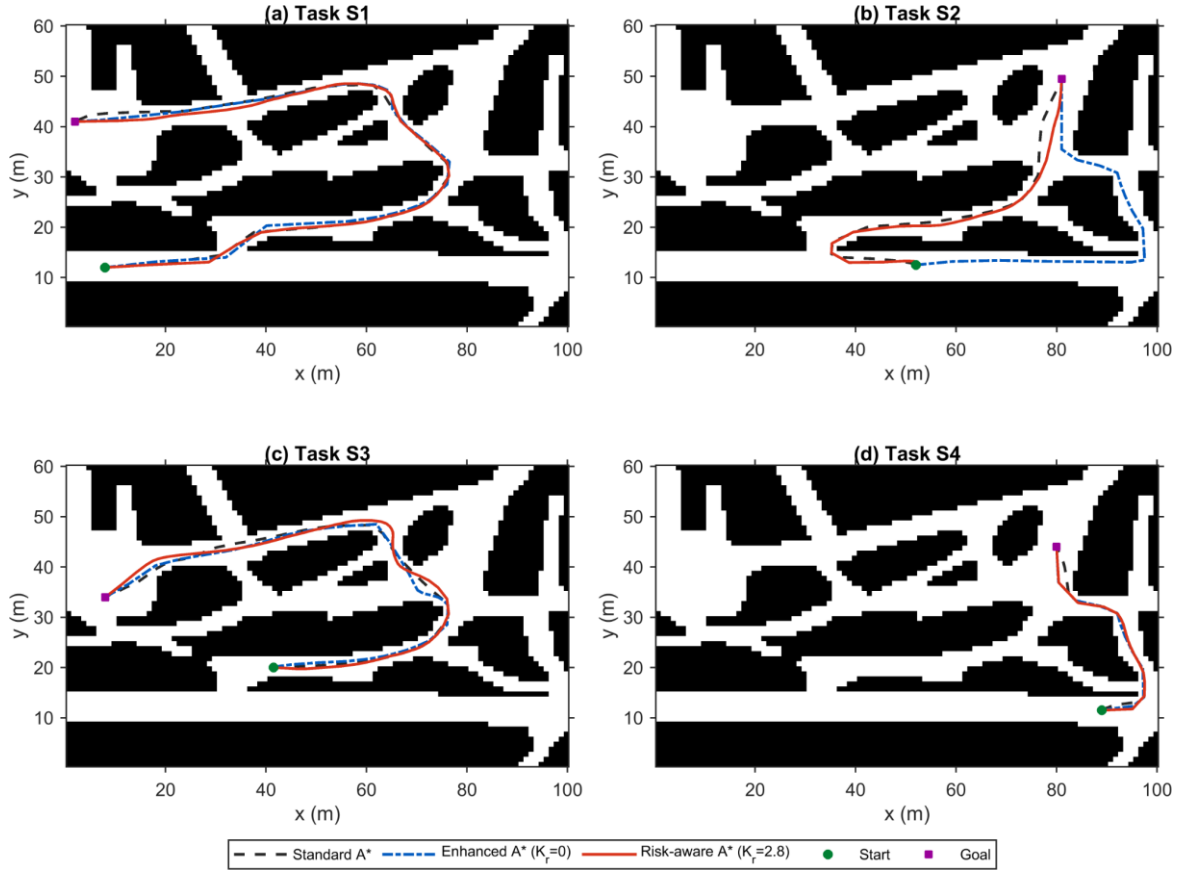


Figure 3. Quantitative comparison across the four planning tasks. a, Path length. b, Mean obstacle-centre distance. c, Path-risk integral. d, Search time. For each task, all three methods use the same occupancy map, start-goal pair and evaluation procedure. Search time in d is the median of five executions for each method and task; the cross-task summary and expanded-node counts are reported in Table 2.

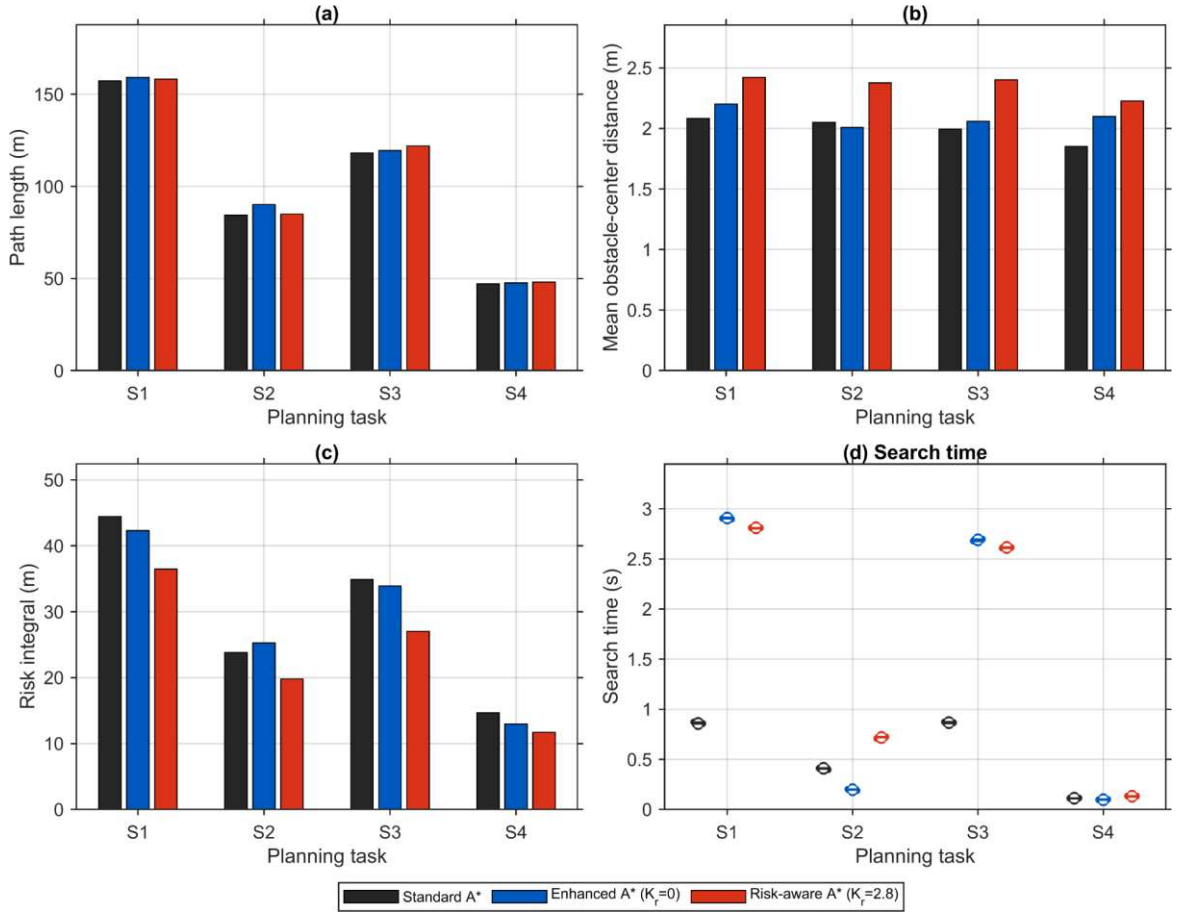


Figure 4. Effect of safety-corridor-constrained B-spline optimization. a, Geometric path before and after B-spline optimization. b, Corresponding absolute-curvature profiles; the dotted horizontal line denotes the planning-curvature limit used for geometric feasibility assessment. Numerical curvature, obstacle-distance and path-length results are provided in Supplementary Table S1.

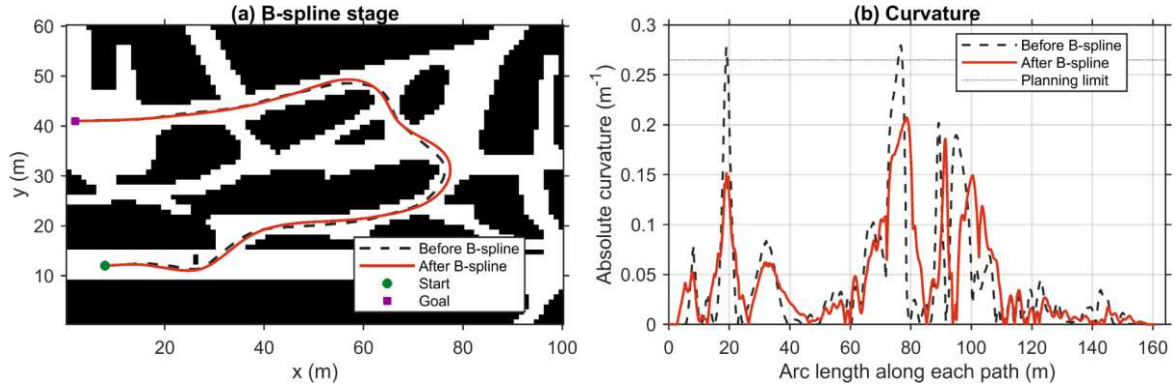


Figure 5. Hierarchical planning around dynamic obstacles. a, Spatial-path evolution through the obstacle events, showing the initial reference, the route after the temporary obstacle and the final path; O1-O3 labels indicate the corresponding event times. b, S-T risk representation on the final path, including warning and occupied boundaries, the constant-speed reference and the final planned trajectory. Conflicts with O1 and O2 are resolved through speed adjustment, whereas O3 triggers local Hybrid A* spatial replanning followed by renewed S-T speed planning.

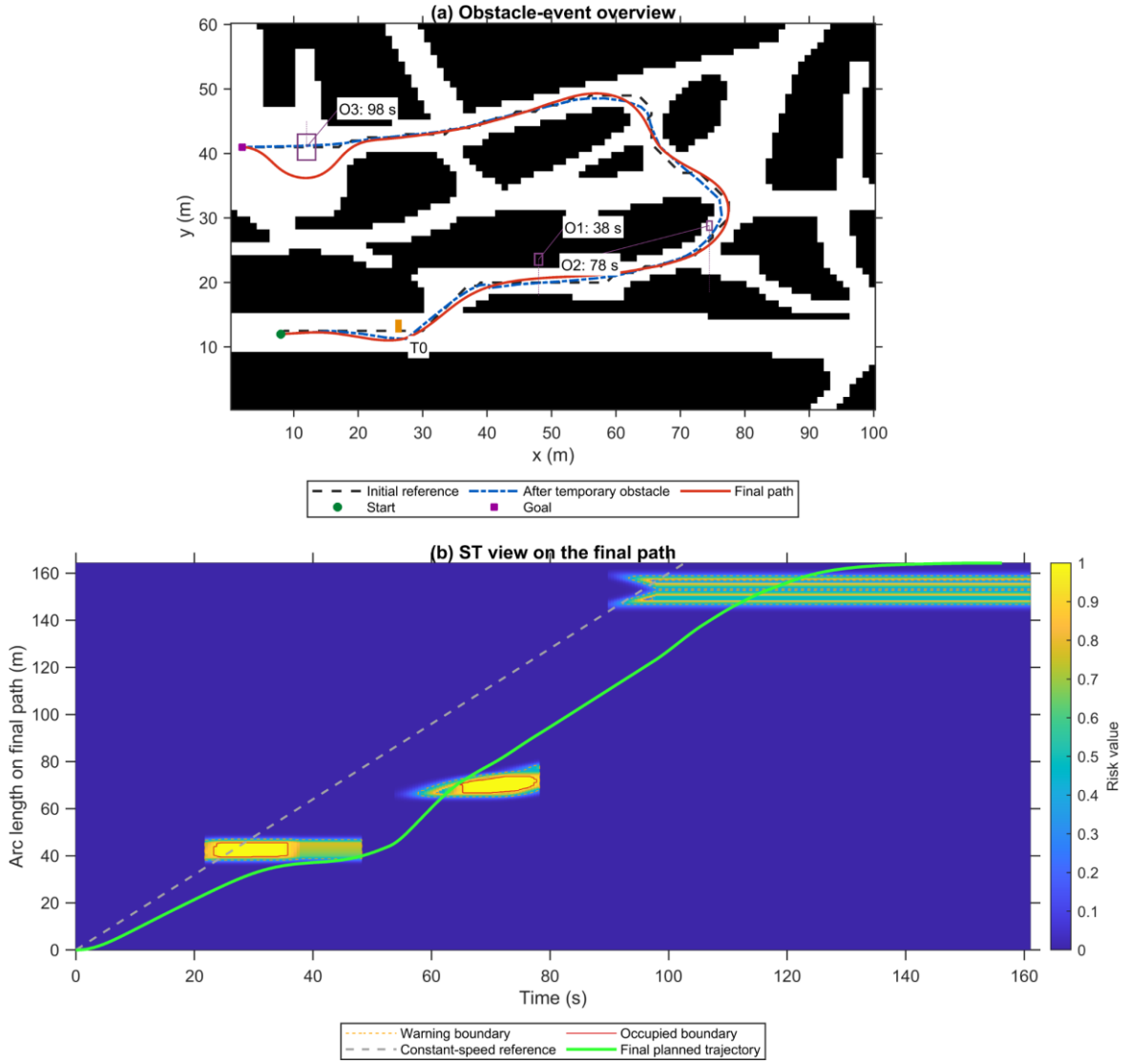
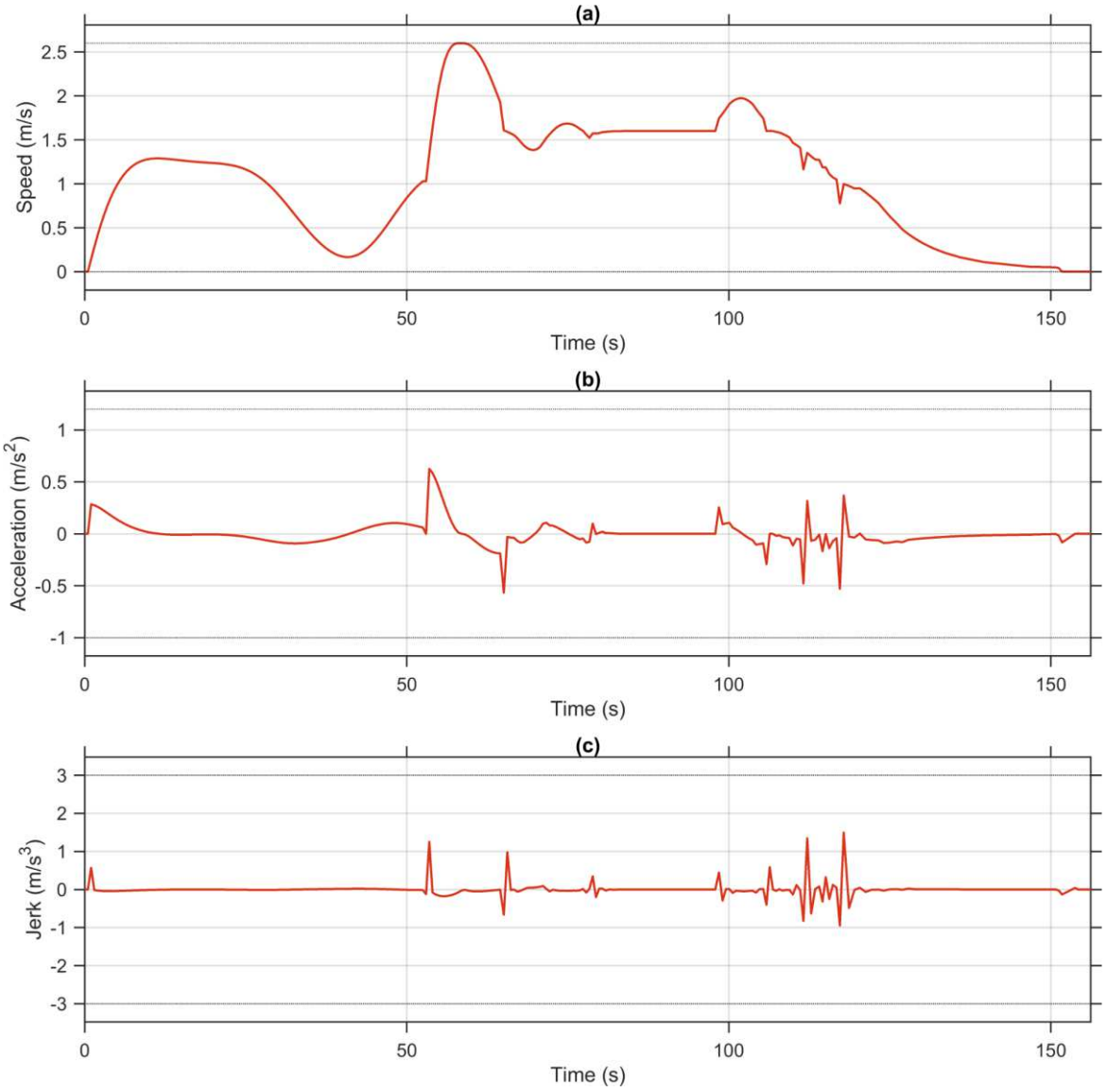


Figure 6. Final planned trajectory kinematics. a, Reference speed. b, Longitudinal acceleration. c, Jerk. Horizontal dotted lines denote the imposed planning bounds. These reference profiles were generated after spatial and S-T planning, before closed-loop CarSim/Simulink tracking validation.



Tables

Table 1. Main vehicle and planning parameters.

Parameter	Symbol	Value
Vehicle length	L_v	3.8 m
Vehicle width	W	1.6 m
Wheelbase	L	2.0 m
Front track	B_f	1.38 m
Grid resolution	Δ	0.5 m/cell
Physical curvature limit	κ_{phy}	0.278852 m^{-1}
Nominal planning curvature limit	κ_{plan}	0.264909 m^{-1}
Hybrid A* curvature limit	κ_{Hybrid}	0.235 m^{-1}
Tracking curvature target	κ_{target}	0.230 m^{-1}
Final curvature limit	κ_{hard}	0.240 m^{-1}
Static obstacle-centre clearance	d_{static}	1.15 m
Dynamic body-boundary margin	m_{dyn}	0.40 m
Cruise speed	v_{ref}	1.60 m s^{-1}
Maximum speed	v_{max}	2.60 m s^{-1}
Maximum acceleration	a_{max}	1.20 m s^{-2}
Maximum deceleration	d_{max}	1.00 m s^{-2}
Nominal lateral-acceleration limit	$a_{y,\text{max}}$	0.50 m s^{-2}
Maximum jerk	j_{max}	3.00 m s^{-3}

Table 2. Cross-scenario path-planning performance.

Metric	**Standard A***	**Enhanced A*** $K_r = 0$	**Proposed** $K_r = 2.8$
Mean path length (m)	101.75	104.12	103.29
Mean minimum obstacle-centre distance (m)	1.1561	1.1563	1.1607
Mean obstacle-centre distance (m)	1.9944	2.0926	2.3572
Risk integral	29.462	28.618	23.754
Mean risk	0.29288	0.27556	0.23227
Expanded nodes	2557.8	3182.0	3561.5
Mean scenario median search time (s)	0.626	1.433	1.555

Path-length, obstacle-distance, risk and expanded-node values are arithmetic means over the four start-goal configurations. Search time is the arithmetic mean of the four scenario-wise medians, with each scenario median obtained from five executions per method. Obstacle-centre distance is measured from the path centreline to obstacle-cell centres.

Supplementary Files

This is a list of supplementary files associated with this preprint. Click to download.

- ScientificReportsSupplementary.pdf